

## Correcting Ionospheric Faraday Rotation for the VLA and MeerKAT

RICHARD A. PERLEY <sup>1</sup>, BRYAN J. BUTLER <sup>2</sup>, ERIC W. GREISEN <sup>2</sup>, BENJAMIN V. HUGO <sup>3,4</sup>, EVANGELIA TREMOU <sup>2</sup>,  
AND A. G. WILLIS <sup>5</sup>

<sup>1</sup>*National Radio Astronomy Observatory, P.O. Box 'O', Socorro, NM, 87801, USA*

<sup>2</sup>*National Radio Astronomy Observatory, P.O. Box 'O', Socorro NM, 87801, USA*

<sup>3</sup>*South African Radio Astronomy Observatory, Liesbeek House, River Park Liesbeek Parkway, Mowbray, Cape Town, 7705 South Africa*

<sup>4</sup>*Rhodes University, Artillery Road, Grahamstown, South Africa*

<sup>5</sup>*Dominion Radio Astrophysical Observatory, P.O. Box 248, Penticton, B.C. V2A 6J9, Canada*

### ABSTRACT

We report here on studies to determine the accuracy of estimated corrections of Ionospheric Faraday Rotation Measure (IFRM) using observations of the Moon with the Very Large Array (VLA) and MeerKAT telescopes. To estimate the IFRM requires an estimate of the total electron content along the line-of-sight to the observed sources (the so-called Slant Total Electron Content, or STEC). Estimating the STEC requires an estimate of the global 2-D map of Vertical Total Electron Content (VTEC) along with the ray path from the telescope to the source. Traditionally, these global VTEC maps have been utilized along with an assumption that the electrons are in a thin shell at a given altitude to provide an estimate of the IFRM as a function of time. We find that this traditional technique significantly overestimates the IFRM – typically by  $\sim 0.5$  to  $1.1$  rad/m<sup>2</sup> for the VLA, and  $\sim -0.3$  rad/m<sup>2</sup> for MeerKAT. Alternatively, the software package ALBUS utilizes raw data from nearby Global Navigation Satellite System (GNSS) stations, to generate a local estimate of the IFRM as a function of time. ALBUS provides considerably better estimates of the IFRM – accurate to  $\sim 0.1$  rad/m<sup>2</sup> for both the VLA and MeerKAT, provided the stations utilized have known receiver bias values. A byproduct of our study is the establishment of the intrinsic electric vector position angle (EVPA) of the standard polarized calibrators 3C286 and 3C138 from 500 MHz to 50 GHz, using additional VLA observations of the Moon, Venus, and Mars.

*Keywords:* Radio interferometry (1346) — Polarimetry (1278)— Calibration (2179)— Earth ionosphere (860)

### 1. INTRODUCTION

Modern interferometric arrays such as the Very Large Array (VLA) and MeerKAT produce full polarimetric visibility data, permitting imaging in all four Stokes parameters I, Q, U, and V. Accurate polarimetry requires establishing the orientation of the electric vector position angle (EVPA) of polarized emission to high accuracy – ideally five degrees or better. Attaining this accuracy requires corrections for a number of instrumental and environmental factors. A major environmental factor at low frequencies is the effect of the Earth’s ionosphere.

As an electromagnetic wave passes through the ionosphere, the polarization angle of the wave undergoes a rotation due to the combined effect of the electrons and the magnetic field. The magnitude of this rotation becomes significant at longer wavelengths (the effect is proportional to wavelength squared), i.e., at long radio wavelengths. This effect is important at frequencies below  $\sim 4$  GHz and is the dominant correction term in observations below  $\sim 1$  GHz.

In order to calibrate polarization observations at these long wavelengths, an estimate of the Ionospheric Faraday Rotation Measure (IFRM) along the line-of-sight to the source being observed as a function of time must be determined. Time-variable global maps of Vertical Total Electron Content (VTEC), produced by a number of organizations, along with an assumption of the vertical distribution of the electrons, the known direction from a telescope to a source, and

a model of the Earth’s magnetic field, can be used to estimate the Slant Total Electron Content (STEC) along the path and hence the IFRM. Accurate polarimetry requires the determination of the IFRM with an accuracy of at least  $0.1 \text{ rad/m}^2$  for  $\lambda \sim 1\text{m}$  on timescales of an hour, or less.

In this paper we describe and compare methods for correcting for the IFRM based on both globally and locally-derived estimates of the STEC, with the goal of determining which of these methods is most accurate and reliable. As part of this work, we have accurately measured the EVPA of the polarization calibrators 3C286 and 3C138 from 0.5 to 50 GHz, using data from the VLA and MeerKAT.

## 2. IONOSPHERIC FARADAY ROTATION

Passage of a linearly polarized electromagnetic wave through a magnetized ionized medium results in a rotation of the plane of polarization given by

$$\Delta\chi = RM\lambda^2 \quad \text{rad} \quad (1)$$

where  $RM$  is the rotation measure, given by

$$RM = 2.62 \times 10^{-17} \int n_e \mathbf{B} \cdot d\mathbf{l} \quad \text{rad/m}^2 \quad (2)$$

with the electron density  $n_e$  in  $\text{m}^{-3}$ , the magnetic field  $\mathbf{B}$  in Gauss, and the propagation path  $\mathbf{l}$  and wavelength  $\lambda$  in meters<sup>1</sup>.

Solar UV and X-ray emissions cause partial ionization ( $\sim 1\%$ ) of the Earth’s atmosphere at heights above  $\sim 100 \text{ km}$ , resulting in daytime electron densities of up to  $10^{12.5}\text{m}^{-3}$  at heights of  $\sim 350 \text{ km}$  during solar maximum, and about an order of magnitude less during solar minimum. Typical night-time densities are about  $10^{11}\text{m}^{-3}$ . Combined with the Earth’s approximately dipolar magnetic field of  $\sim 1 \text{ Gauss}$ , the resulting typical night-time IFRMs at the VLA and MeerKAT sites have a magnitude of  $\sim 0.5 \text{ rad/m}^2$ , with daytime values between 2 and 6  $\text{rad/m}^2$ , (positive for the VLA, negative for MeerKAT) depending on solar activity and source direction. In addition to the regular day–night variations, significant variations on hourly, or shorter, timescales are common, especially during periods of significant solar activity.

## 3. ESTIMATING THE IFRM

### 3.1. Using Global VTEC Maps

Correction of the ionospheric Faraday rotation requires knowing the electron density and magnetic field distributions along the propagation path from the source to the observer at the time of observation – a difficult prospect. Because of this, simpler approximations utilizing available global vertical total electron content (VTEC) maps defined as a function of longitude, latitude and time, a model of the magnetic field, and a thin-shell approximation for the distribution of the ionospheric electrons have been developed. These global VTEC map files are developed by various Ionospheric Associated Analysis Centers (IAACs) of the International GNSS (Global Navigation Satellite System) Service (IGS), using timing data from up to four GNSS constellations (GPS, Galileo, BeiDou, and GLONASS) and a network of globally distributed stations. The timing referred to here is the additional delay caused by the ionosphere to signals broadcast by the satellites. For signals propagating through an ionized medium, this additional, dispersive group-path delay is proportional to the product of the electron column density and the wavelength squared:  $\Delta T \propto TEC \times \lambda^2$ . For two frequencies, analysis (R. S. Lawrence et al. 1964) shows the column density (called the ‘tau-TEC’) is related to the difference in propagation times by

$$TEC_{TU} = 6.75 \times 10^{-2} \frac{\Delta T}{\lambda_1^2 - \lambda_2^2} \quad (3)$$

where the time difference  $\Delta T$  is in nsec, the wavelength  $\lambda$  is in meters, and the units of TEC are in TUs, defined as  $1 \text{ TU} = 10^{16} \text{ electrons/m}^2$  (W. C. Erickson et al. 2001). For the GPS system,  $\lambda_1 = 0.1904 \text{ meters}$ , and  $\lambda_2 = 0.2444 \text{ meters}$ . With these values, the relation between the dispersive delay and the path TEC in TU units is  $TEC_{TU} = 2.853\Delta T$ .

<sup>1</sup> This simple relation holds when there is neither polarized emission nor absorption in the rotating medium and when the frequency of observation is much higher than the plasma frequency (typically 12 MHz) and the gyro frequency (typically 1.4 MHz) – conditions which apply to the Earth’s ionosphere and the observations reported in this paper.

**Table 1.** Global VTEC Map Characteristics

Name	Organization	ElCutoff	#Satellites	SatCon	#Stations	TimeStep
jplg	Jet Propulsion Laboratory	10	32	G	170	2hr
codg	Center for Orbit Determination in Europe	10	79	G,E	235	1
esag	European Space Operations Center	10	78	G,E	248	2
igsg	Geodynamics Research Lab,GRL/UWN	0	31	G	297	2
upcg	Polytechnic Univrsity of Catalonia	0	54	G,E	235	2
casg	Chinese Academy of Science	0	108	G,C,E,R	?	0.5
emrg	Space Weather Canada	10	52	G,R	270	1

NOTE—Explanation of Satellite Constellations: G: US Global Positioning System (GPS, 32 satellites); E: European Union Galileo (24); C: China BeiDou Navigation Satellite System (24); R: Russian Global Navigation Satellite System (GLONASS, 24)

A much more accurate estimation of the TEC is obtained from the relative phases of the carrier frequencies,  $\Delta\phi$ . In this case, the column density (called the ‘phase-TEC’) is related to this phase by

$$TEC_{TU} = 6.28 \times 10^{-4} \frac{\Delta\phi}{\lambda_1 - \lambda_2} \quad (4)$$

where the phase difference is in degrees, the wavelength in meters and TEC in TEC units. For the GPS system, the relation between the carrier phase difference and the path TEC is  $TEC_{TU} = 1.16 \times 10^{-2} \Delta\phi$ . Although this estimate is subject to full cycle ambiguities, current software (including the ALBUS program discussed later in this paper) utilizes the tau-TEC estimates to detect and remove these ambiguities.

Many institutions generate VTEC maps using different combinations of the four available global satellite constellations and ground stations. These global maps are typically produced on a 2.5 by 5 degree grid (latitude, longitude) on timescales of 30 minutes to 2 hours. Table 1 gives typical characteristics of seven available VTEC maps. These maps are then interpolated in time and space to generate the desired STEC values in the direction of interest needed for the calculation of the IFRM.

Efforts to estimate IFRM corrections for the VLA began in the 1990s with the implementation of the P-band (330 MHz) receivers and the public availability of the VTEC maps. [W. C. Erickson et al. \(2001\)](#) described VLA observations of the polarized pulsar PSR 1932+109 taken in the late 1990s. They compared the observed pulsar EVPA to predictions derived by utilizing timing data from a GPS receiver temporarily placed at the center of the VLA, concluding that IFRM corrections accurate to 0.2 rad/m<sup>2</sup> were possible. As a result of this investigative effort, the program TECOR in the software package AIPS ([E. W. Greisen 2003](#)) was implemented in 1998 to generate IFRM estimates utilizing published global maps of the vertical total electron content available from the CDDIS (Crustal Dynamics Data Interchange System) and a model of the Earth’s magnetic field ([S. Chapman & J. Bartels 1940](#); [P. Alken et al. 2021](#)), assuming the electrons are all in a thin shell at a height of 450 km. This height is assumed because it is roughly the appropriate height for a thin-shell approximation over a wide variety of conditions and in mid-latitudes ([Q. Zhao et al. 2019](#)).

There are two alternative programs known to us which provide IFRM estimates – `ionFR` ([C. Sotomayor-Beltran et al. 2013](#)) and `RMextract` ([M. Mevius 2018](#)). Both of these programs work similarly to TECOR, i.e., using the same model of the Earth’s magnetic field, thin-shell approximation, and global VTEC maps. `ionFR`<sup>2</sup> is no longer maintained. `RMextract` has recently been superseded by `spinifex`<sup>3</sup> ([M. Mevius et al. 2025](#)), which is under development for use with LOFAR and SKA-LO observations, both of which operate at wavelengths longer than 1 meter. In Appendix A we show comparisons of `RMextract`, `TECOR`, and `spinifex` for a particular observation.

<sup>2</sup> <https://github.com/csobey/ionFR>

<sup>3</sup> <https://git.astron.nl/RD/spinifex>



**Figure 1.** Locations of the GNSS stations for the VLA (left) and MeerKAT (right) potentially utilized by ALBUS are shown by the small dots. The larger blue dots show the locations of the two arrays.

### 3.2. Using Locally-Derived Estimates of the STEC

An alternative to utilization of global VTEC maps is a regional model provided by the ALBUS program (Advanced Long Baseline User Software)<sup>4</sup> (Willis, A. 2022), written to estimate dispersive delays for VLBI phase corrections, and subsequently modified to provide estimation of the STEC for a given location and direction as a function of time. ALBUS offers ten models, labelled ‘G00’ through ‘G09’, including both ‘2-D’ (thin-shell) and ‘3-D’ electron density distributions.

The ALBUS program calculates IFRM estimates by utilizing GNSS timing data from ground stations within a specified distance of a given location combined with, for the 3-D models, a parametrically generated ionospheric vertical distribution of electrons. For both the VLA and MeerKAT, there are typically up to  $\sim 20$  potential GNSS stations within a 300 km radius whose data can be used to generate an estimate of the STEC. The locations of these stations utilized for this paper are shown in Fig 1 for both the VLA and MeerKAT arrays. The ALBUS program is available stand-alone, or can be executed within AIPS through the use of a container. Although ALBUS knows of three satellite constellations, at present it utilizes only the GPS system data.

We have extensively tested the results of these models on our data, the details of which are in Appendix B. The summary conclusion is that the 2-dimensional ‘G01’ model, when utilizing the closest GNSS station for which the timing bias value is known, provides the best estimate of the IFRM for both the VLA and MeerKAT. For the rest of this paper, when utilizing the imaging results including IFRM corrections, we have used the G01 model.

## 4. SOLAR SYSTEM BODIES AS EVPA CALIBRATORS

A proper assessment of the accuracy of an estimation of the IFRM requires observations of a source of *a priori* known EVPA. This is required because, as will be shown in subsequent sections, although all IFRM estimates based on the global VTEC maps are effective in removing the day to night change in the IFRM, they also generate (at least for the VLA and MeerKAT) a significant overestimation of the VTEC, resulting in an overcorrection of the IFRM rotation.

The standard set of strongly polarized calibrator sources (such as 3C286 and 3C138) are not sufficient for the purpose of assessing the accuracy of these corrections for two reasons. First, their intrinsic EVPA values are a function of frequency, and are not known at the frequencies where ionospheric Faraday rotation becomes important, so that one cannot determine if an IFRM-corrected image provides the correct EVPA. Secondly, they are completely depolarized at frequencies below 500 MHz, where the ionospheric Faraday rotations become especially important. An additional point is that, with the exception of 3C286, compact polarized sources are time-variable in both total and polarized flux density on timescales of weeks to years. Similarly, although observations of pulsars have been successfully used to judge diurnal IFRM correction accuracy (see, N. K. Porayko et al. 2019; N. K. Porayko et al. 2023) they cannot be used to judge the accuracy of the corrected EVPA, since their intrinsic EVPA values are not known.

<sup>4</sup> [https://github.com/twillis449/ALBUS\\_ionosphere/blob/master/twillis\\_ALBUS\\_paper.pdf](https://github.com/twillis449/ALBUS_ionosphere/blob/master/twillis_ALBUS_paper.pdf)

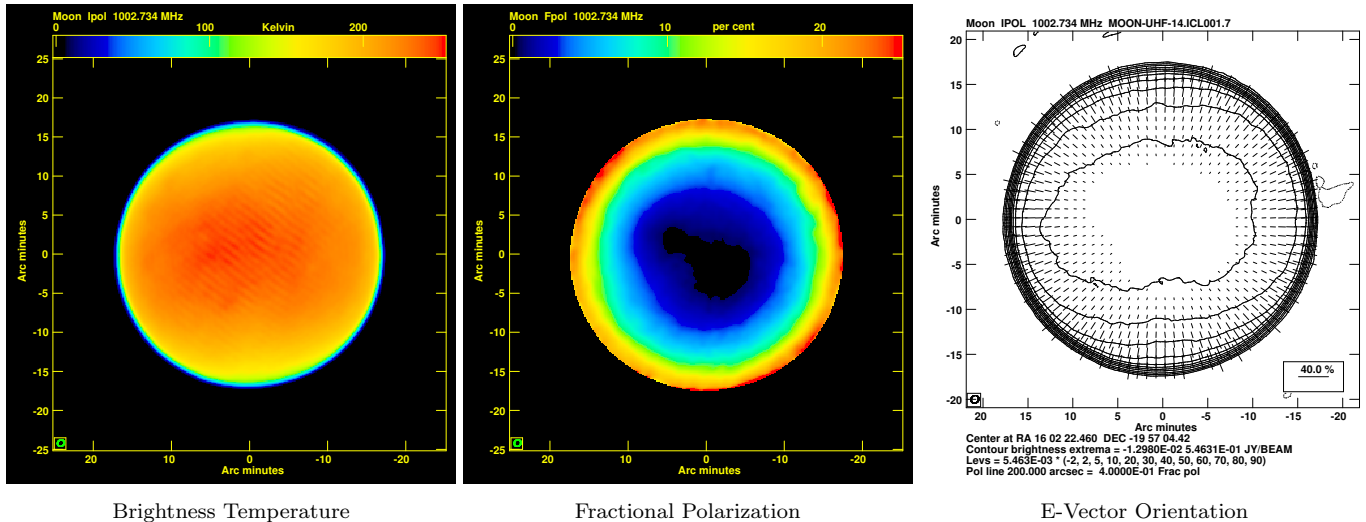


**Figure 2.** Color-coded MeerKAT images of the Moon at 1002 MHz. The Stokes I brightness (left) is nearly featureless while the fractional polarized brightness (center) is strongly peaked toward the limb, with fractional polarization reaching 30% near the lunar limb. The EVPA vectors (right) are nearly radial. The slight ripple seen in the Stokes I image is from a deconvolution instability.

To our knowledge, sources of wideband polarized radio emission with *a priori* known EVPA distributions that are useful (have enough flux density, are the proper size, etc.) are limited to the Moon and the planets Mercury, Venus, and Mars. For these objects, the originally unpolarized thermal radio emission originates from  $10 - 20 \lambda$  below the surface, and becomes linearly polarized due to differential refraction of the orthogonal planes of polarization upon passage through the planetary surface. The physical principles which cause this polarization are discussed by C. E. Heiles & F. D. Drake (1963) and R. A. Perley & B. J. Butler (2013a). The resulting observed emission is highly polarized near the limb of the body with a nearly perfect radial orientation. A good example of lunar polarimetric images using data taken with MeerKAT is shown in Fig. 2.

Imaging of the polarized thermal emission of these extended objects is difficult, especially at frequencies below 2 GHz, as their surface brightnesses and flux densities decline with the square of the frequency. The observational requirements for effective planetary polarimetry are that the Stokes I surface brightness be sufficiently high that the detected flux density within the array resolution beam has an SNR of at least 20 on a timescale comparable to any ionospheric variations, and that there be at least three, and preferably more than five resolution elements across the source. The result of these two requirements for VLA observations is that only the Moon can be used at frequencies below 1 GHz, and only when the VLA is in its compact D or C configurations. Additionally, the 25-meter diameter of the VLA antennas limits lunar polarimetry to frequencies below 1.5 GHz. For higher frequency work, Mars can be utilized for polarimetry at frequencies above 4 GHz, and Venus for frequencies between 1 and 10 GHz (the upper limit being due to absorption in the Venusian atmosphere).

For MeerKAT, only the Moon can be utilized for polarimetric studies, as the array resolution is too low for the other planets. The high central concentration of MeerKAT stations, and the 13.5 meter antenna diameter, make this array ideal for lunar polarimetric observations in its lowest two frequency bands.

The VLA's sensitivity in P-band is significantly degraded by strong mutual coupling between the antennas on baselines less than  $\sim 500$  m, and by a poor RFI environment due to various satellite and local transmissions. Nearly 50% of the bandwidth is lost for observations in the compact C and D configurations due to RFI. The result of these factors is that on-source integrations of at least 10 minutes are required to obtain sufficiently good polarimetric sensitivity for lunar observing at 300 MHz. These issues are not a problem for VLA observations at higher frequencies thanks to interferometer fringe-winding attenuating the RFI and mutual coupling, nor for the MeerKAT array, for which careful design has virtually eliminated detectable signal coupling between antennas. The isolated location of the MeerKAT array combined with tight control of local sources of RFI result in less than 5% of the bandwidth being lost to RFI in the UHF band.

**Table 2.** VLA and MeerKAT Band Codes

Array	BandCode	Freq. Range (GHz)	Array	BandCode	Freq. Range (GHz)
VLA	P	0.23 – 0.45	VLA	K	18 – 28
VLA	L	1.0 – 2.0	VLA	A	28 – 40
VLA	S	2.0 – 4.0	VLA	Q	40 – 50
VLA	C	4.0 – 8.0	MeerKAT	UHF	0.54 – 1.10
VLA	X	8.0 – 12.0	MeerKAT	L	0.85 – 1.70
VLA	Ku	12.0 – 18.0	MeerKAT	S0	1.75 – 2.62

## 5. OBSERVATIONS

Multiple observations at multiple frequency bands have been taken with the VLA and MeerKAT for this program. We utilize ‘band codes’ to simplify presentation and discussion of the results. Table 2 gives the band codes and frequencies spanned by the VLA and MeerKAT receivers used in this study.

Accurate assessment of the IFRM corrections requires multiple extended observations of the planetary bodies, especially at the lower frequencies where the emission is weakest and IFRM rotation corrections are large. We have thus observed the Moon with the VLA on 10 occasions, and with MeerKAT on six, as listed in Table 3. In this table, column #4 gives an observation code which is extensively used in the following sections to concisely identify which observation is being discussed.

VLA observations of the planets Venus and Mars, used to establish the high-frequency EVPA for 3C286 and 3C138, are summarized in Table 4.

Editing and calibration of all data were done using the AIPS software package using well-established procedures for calibration utilizing the parallel-hand correlations. Polarimetry requires calibration of the cross-hand correlations, the details of which differ between linearly and circularly polarized systems. The VLA’s high frequency receivers utilize circularly polarized receivers, while MeerKAT and the VLA’s P-band receivers utilize linearly polarized receivers. In the following paragraphs, we detail the procedures.

For both linear and circular systems, calibration of the antenna cross-polarization (so-called D-terms) was done using known unpolarized sources, for which the procedure is the same. We utilized 3C84 for the VLA high-frequency observations, 3C147 (J0542+4951) for the VLA’s P-band observations, and J0408-6545 or J1939-6342 for the MeerKAT observations.

The critical difference between circularly-polarized and linearly-polarized receivers is the effect of a cross-hand phase offset between the parallel-hand channels which causes rotation between the Stokes parameters. Standard parallel-hand calibration references the opposite hand phases (R and L, or H and V) to those of the chosen reference antenna. The phase difference between the parallel-hand receivers of this antenna is imprinted on all cross-hand correlations. For circularly-polarized system, a residual phase offset of  $\delta\phi$  is manifested by a rotation between Stokes Q and U by an angle  $\delta\chi = 0.5\delta\phi$ . For linear systems (after correction for the antenna parallactic angle), the rotation is between Stokes U and Stokes V<sup>5</sup>.

In both cases, correction of these phase offsets requires either an on-board cross-hand calibration system, or observations of a strongly polarized source. The VLA does not have an on-board cross-hand calibration system, so an observation of a strongly polarized source of known EVPA is required for determination of this cross-hand phase offset for its circular-based receivers. The stable highly polarized source 3C286 is most commonly utilized for this purpose.

For linear systems, we take advantage of the fact that these polarized sources have negligible circularly polarized emission, and utilize the V=0 method detailed in Perley, R. et al. (2022, EVLA Memo 219). The sources utilized were DA240, 3C303, or 3C345 for the VLA’s P-band observations, and either 3C286 or 3C138, both of which remain sufficiently polarized down to 544 MHz, for the MeerKAT observations.

<sup>5</sup> These rotations are best understood as rotations in the Poincaré sphere about the V axis for a circular system, and about the Q axis for a linear system.

**Table 3.** Polarimetric Lunar Observations with the VLA and MeerKAT

Date	Array/Config	Band	Code	Polarized Sources	Separation	IFRM Range	ToS
					Degrees	rad/m <sup>2</sup>	min
10 May 2017	VLA-D	P	D1	DA240, 3C345	T171	0.4 – 0.7	9x15
06 Aug 2017	VLA-C	P	C1	3C345	T162	0.6 – 1.4	56x5
30 Dec 2018	VLA-C	P	C2	DA240, 3C303, 3C345	L75	0.3 – 1.5	58x8
31 May 2021	VLA-D	L	L1	3C286, 3C138	L112	0.3 – 2.4	18x20
22 Jun 2021	MeerKAT	UHF	U1	3C286	T150	−0.10 – −0.04	17x10
26 Jun 2021	MeerKAT	S0	MS	3C286	L156	−0.10 – −0.05	16x10
18 Aug 2021	MeerKAT	L	ML	3C286	T128	−0.25 – −0.15	19x10
20 Sep 2022	VLA-D	L	L2	3C286, 3C138	L59	1.4 – 2.3	30x10
13 Dec 2022	VLA-C	P	C3	DA240, 3C303, 3C345	L122	0.3 – 1.2	32x10
04 Nov 2023	VLA-D	P	D2	DA240	L100	0.4 – 2.4	14x5
20 Jan 2024	VLA-D⇒C	P	DC	DA240	T125	0.5 – 2.5	22x10
09 Mar 2025	VLA-D	P	D3	DA240, 3C303, 3C345	T120	0.5 – 2.7	13x1.5
09 Mar 2025	VLA-D	L	L3	DA240, 3C303, 3C345	T120	0.5 – 2.7	13x3
18 Aug 2025	MeerKAT	UHF	U2	3C138	L64	−2.5 – −0.4	23x8
19 Aug 2025	MeerKAT	UHF	U3	3C138	L51	−3.0 – −0.3	23x8
19 Aug 2025	VLA-C⇒B	P	CB	DA240	L46	0.3 – 2.4	19x14
30 Oct 2025	MeerKAT	UHF	U4	3C286	T100	−0.7 – −2.1	18x8

NOTE—**Separation:** The angular offset between the Moon and the Sun. ‘T’ means the Moon trails the Sun, ‘L’ means the Moon leads the Sun. **ToS:** Time on Source, given as the number of observations times the duration of each in minutes. Proposal codes for the MeerKAT data are EXT-20220902-BH-01 for the 2021 and 30 Oct 2025 observations, and EXT-20220615-BH-01 for the August 2025 observations.

**Table 4.** Planetary Observations with the VLA

Date	Config	Bands Used	Planet	Solar Separation	IFRM Range	Ang.Size
				Degrees	rad/m <sup>2</sup>	arcsec
03 Mar 2022	A	L, S	Venus	45	1.2 – 3.0	30
14 Apr 2022	A	C, X	Mars	35	0.6 – 4.5	5.4
31 Jan 2025	A	L, S	Venus	45	2.0 – 4.5	32
31 Jan 2025	A	C, X, U	Mars	158	0.5 – 1.3	13.
09 Mar 2025	D	S, C, X	Venus	21	3.4 – 5.1	55
09 Mar 2025	D	U, K, A, Q	Mars	118	0.5 – 3.0	10.0

NOTE—The 2025 observations included all bands, but only those shown in the table could be used for this work due to array resolution or sensitivity limits. Venus cannot be used above 10 GHz due to absorption in its atmosphere.

Conversion of the linearly-polarized MeerKAT data to a circular basis was done as described by [Perley, R. & Greisen, E. \(2024, EVLA Memo 229\)](#), in order to enable better calibration using linearly polarized calibrator sources<sup>6</sup>.

<sup>6</sup> This conversion was not needed for the linear-polarized VLA P-band data, since all calibrators utilized for these observations are known to be unpolarized.

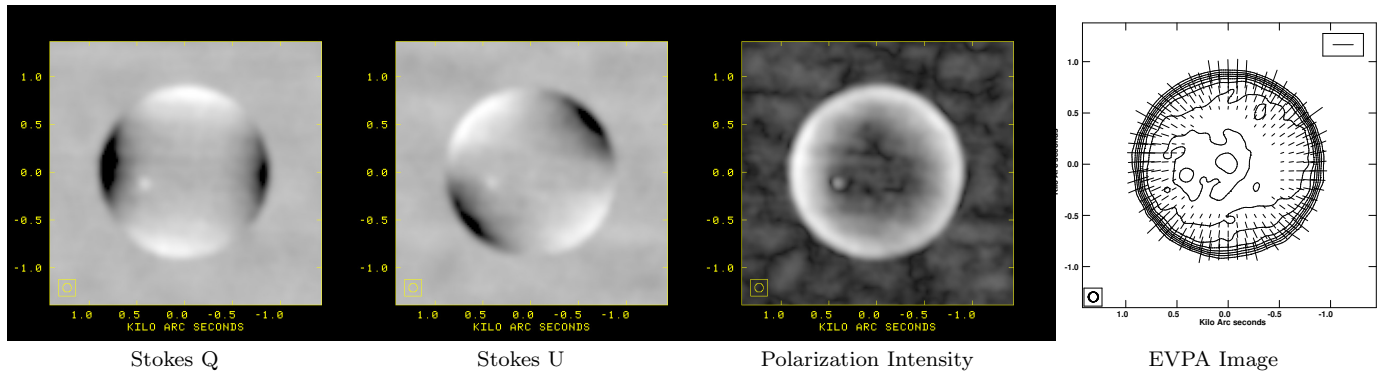


**Figure 3.** Showing the image products from the C3 observation. The bright spot in the three leftmost panels is due to reflection of solar emission.

The ALBUS G01 model, using data from the nearest well-calibrated GNSS station (‘pie1’ for the VLA, and ‘suth’ for MeerKAT) was used to estimate the IFRM for all frequencies up to 4 GHz.

Imaging was done utilizing the AIPS task IMAGR, applying the various estimates of the IFRM on timescales appropriate to tracking the changes in the EVPA. An example of the lunar images from the VLA ‘C3’ observation is shown in Fig. 3. The prominent emission spot seen in the Q, U, and polarized intensity image is due to reflected solar emission, which is orthogonally polarized to the lunar thermal emission.

As noted in Section 4, the intrinsic EVPA distribution for the moon and planets is known to be radial – providing the image resolution is lower than the scale size of planetary features. An incorrect removal of the ionospheric rotation – or an error in the data calibration or image processing – will show up as an offset of the observed EVPA from radial around the limb of the polarization image. To obtain a quantitative measure of this rotation, the AIPS program MARSP was used to determine the mean and standard deviation of the EVPA offset from radial for circularly symmetric objects. The program permits specification of the minimum brightness between the inner and outer radii of an annulus within which the data are to be included for processing.

## 6. VLA RESULTS

The procedure for determining the accuracy of the various IFRM estimates was to generate both uncorrected and IFRM-corrected lunar polarization images as a function of time and frequency, applying different estimates of the IFRM. These images were then analysed for the mean offset from the known intrinsic radial EVPA.

Examples of the IFRM estimates generated by the ‘jplg’ VTEC maps are shown in Fig 4 for six of the P-band VLA lunar observations. The red traces in each panel show the IFRM estimates for the Moon. The polarized calibrator IFRM estimates are shown in color – blue for DA240, purple for 3C303, and green for 3C345. Of these six observations, the last two – ‘D2’ and ‘DC’ – proved the most useful for our study, as these observations spanned sunrise or sunset, and the changes in IFRM during the observation period were larger and smoother than in the other observations.

### 6.1. IFRM Estimation

In this section we address the question of how well the various IFRM estimates correct the observed lunar EVPAs. In Fig. 5, we show three global and one ALBUS lunar IFRM estimates for the ‘D2’ and ‘DC’ observations. The three global estimates are based on the ‘jplg’, ‘upcg’, and ‘codg’ global maps, and are chosen to show the range of estimates from all seven that we investigated. The displayed ALBUS estimate is the G01-pie1 (single GNSS station using the ‘pie1’ GNSS station).

It is immediately evident from the figure that the IFRM estimates based on global VTEC maps are significantly higher than the local ALBUS estimates. Importantly, the *change* in IFRM from night to day for all models is nearly the same. Evidently, the globally-derived estimates have an IFRM offset with respect to the local estimates. There is enough sensitivity in the lunar observations for the ‘D2’ and ‘DC’ observations that we can measure the lunar IFRM as a function of time. These values are shown as individual data points, with errors determined from the dispersion in the EVPA values. For both days, the ALBUS G01 estimates are a far better match to the measured values than the global estimates.

hbt

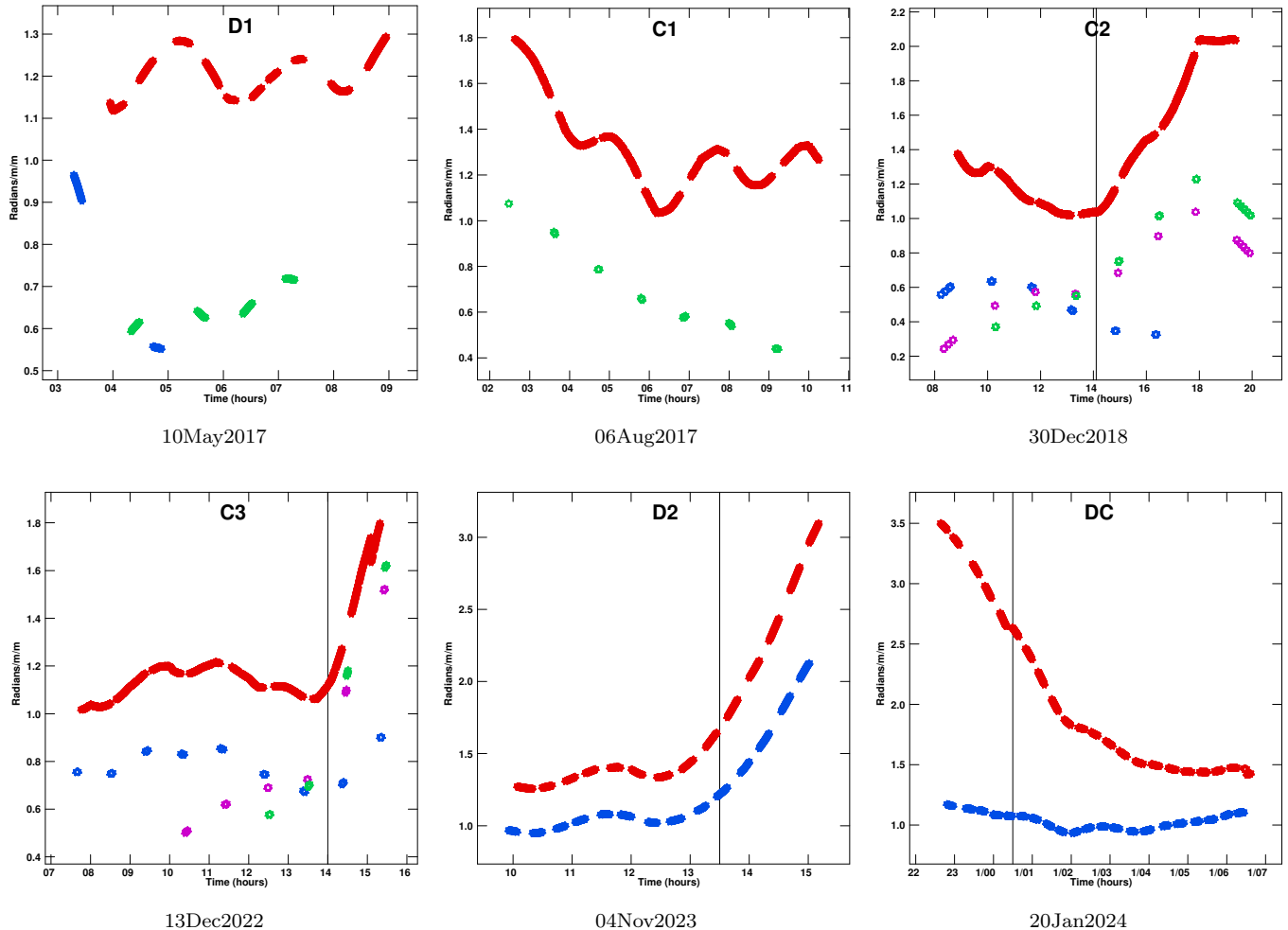


**Figure 4.** Examples of the estimated lunar IFRMs by TECOR, using the ‘jplg’ global VTEC maps. Time is in UTC hours – subtract seven for local MST. Sources are color-coded: red for the Moon, blue for DA240, purple for 3C303, and green for 3C345. The vertical line indicates time of local sunrise or (for the DC observation) sunset.

The conclusions noted above hold equally for all eight VLA lunar P-band observations: The global IFRM estimates are always higher than the local ALBUS estimates, and higher than the observed IFRM values. This IFRM offset is nearly constant over the duration of a single observation, but differs significantly between observations.

Time-sequenced determinations of the lunar IFRM were only practical with the ‘D2’ and ‘DC’ observations, as only these two spanned the day-night transition with a significant change in IFRM. However, since the major difference between the global and local estimates is a constant, so that all IFRM estimates are equally effective in removing the *change* in the day to night IFRM, lunar polarimetric imaging utilizing all the data from a given observation is very effective in investigating which estimate is best. These integrated images have excellent sensitivity, providing accurate estimates of the residual IFRM following correction by any individual IFRM estimate.

The results of doing this are shown in Fig 6 for six of the eight VLA observations. Here we show the post-IFRM corrected EVPA offsets as a function of  $\lambda^2$  for the lunar observations, along with a linear least-squares fit. Color-coding in the figure is the same in each panel: G01-pie1 (single nearby station) in green, global-jplg in yellow, global-upcg in maroon, and global-codg in turquoise. The three global estimates displayed were chosen to span the range of estimates – all other global VTEC map-based estimates are similar except for their offsets.

The excellent linear fits to these data demonstrate that the residuals are due to an overestimation of the IFRM, and are not due to an offset in EVPA. The three estimates based on global VTEC maps always significantly overcorrect the IFRM (resulting in a negative slope), while the IFRM estimate based on the G01 ALBUS model results in EVPA

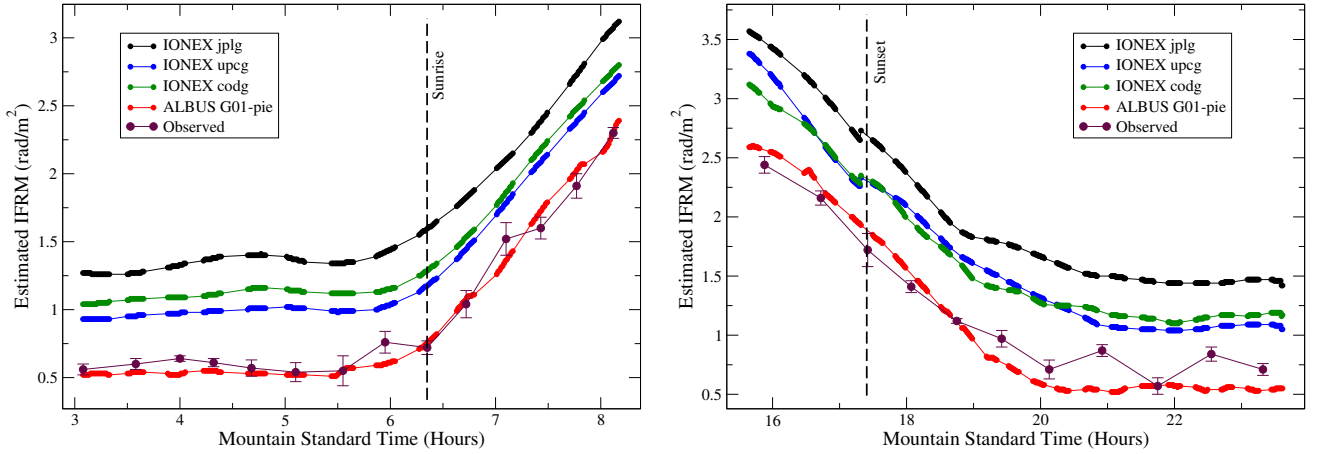


**Figure 5.** The lunar IFRM estimates from three global and two local models, for the ‘D2’ observation (left) and the ‘DC’ observation (right). The three displayed global estimates are representative of all seven global maps we have investigated. The vertical dashed line marks sunrise or sunset. The plotted data points (in maroon, with error bars) are the actual IFRM values determined from the lunar observations.

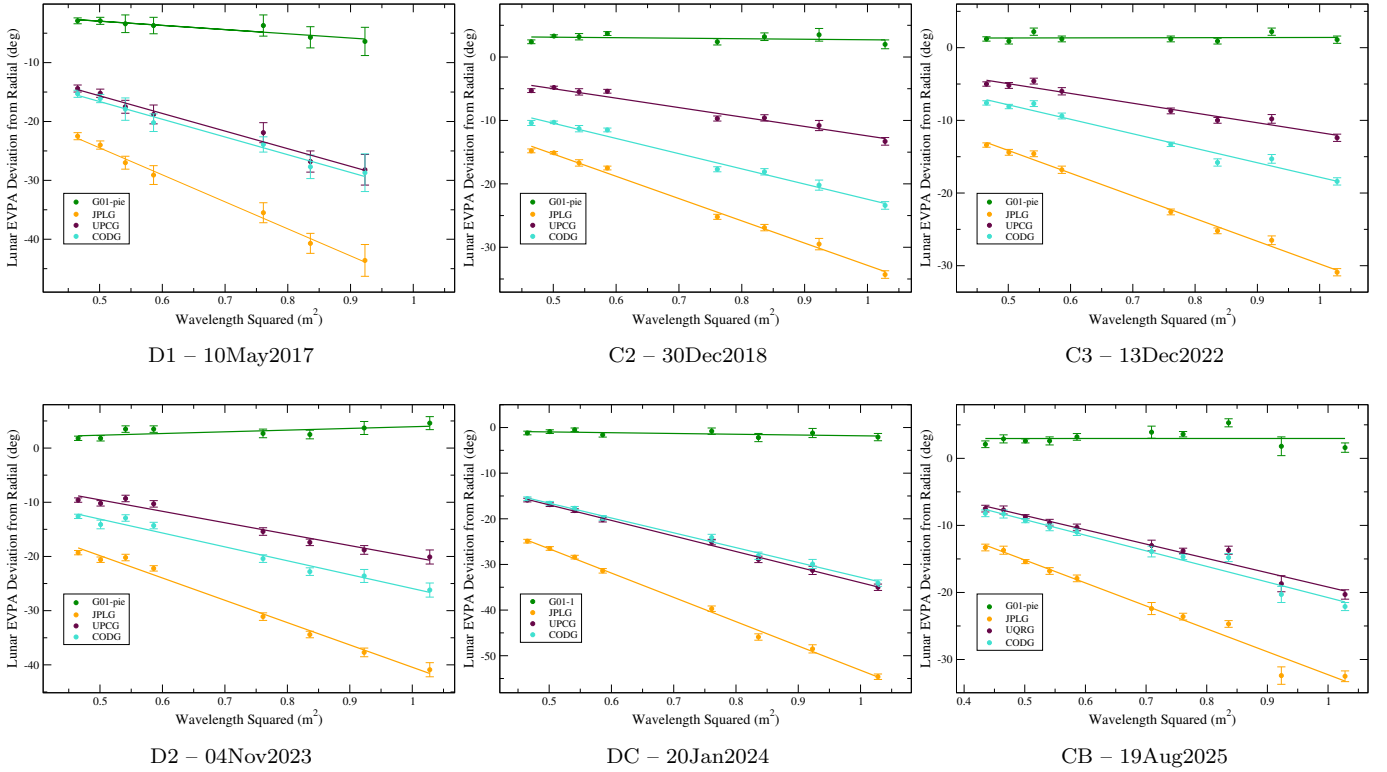


**Figure 6.** The lunar EVPA measurements following correction by four IFRM estimates, the G01-pie1 estimate from ALBUS and three from global VTEC maps: G01-pie1 in green, global-jplg in yellow, global-upcg in maroon, and global-codg in turquoise. The global estimates always significantly overestimate the correction, the ALBUS G01 model is always the best.

values with close to zero slope. For all data shown, a linear fit of the residual EVPAs against  $\lambda^2$  was done, the results of which are shown by the straight lines. The slopes are the residual IFRMs.

The parameters of these linear fits to the post-correction EVPAs are shown in Table 5. ‘G01-pie1’ is the G01 model, using only the nearest GNSS station ‘pie1’ (the VLBA Pietown location).

Key points to note are:

**Table 5.** Fit Parameters for all P-band Lunar Observations

Code	G01-piel		global-jplg		global-upcg	
	Slope	Int.	Slope	Int.	Slope	Int.
	rad/m <sup>2</sup>	Deg	rad/m <sup>2</sup>	Deg	rad/m <sup>2</sup>	Deg
D1	-0.12± .02	-0.6± 0.9	-.80± .03	-1.5± 1.2	-.52± .04	-0.7± 1.5
C1	±	±	-.65± .02	-2.2± 0.9	-.25± .02	-2.0± 0.9
C2	0.01± .02	3.5± 0.8	-.61± .02	2.3± 0.8	-.26± .02	2.4± 0.9
C3	0.00± .02	1.3± 1.0	-.54± .02	1.5± 0.8	-.23± .02	1.8± 0.8
D2	0.05± .02	0.8± 1.0	-.71± .03	0.7± 1.3	-.37± .03	1.0± 1.1
DC	-0.03± .02	-0.1± 0.7	-.93± .02	0.0± 1.0	-.60± .01	0.1± 0.5
D3	-0.10± .04	1.2± 1.6	-.68± .04	1.8± 1.7	-.23± .07	2.4± 2.8
CB	0.00± .03	3.0± 1.3	-.60± .03	1.9± 1.4	-.37± .02	2.1± 1.0

NOTE—The G01-piel fit for the ‘C1’ observation is missing as the GNSS station data for this observation were corrupted.

- Application of all IFRM estimates results in close to zero intercepts. Each estimate, for a given day, gives the same zero-wavelength intercept, to within the errors. The small offsets seen (for example, the four intercept estimates for the D2 observation have an average offset of about 1 degree) are attributed to the misorientation of the reference antenna receiver feeds – these offsets are well within the error tolerance of orienting the dipoles.
- The observed residual slopes for the three global estimates vary considerably between observations. The ‘jplg’ residuals vary from  $-0.54$  to  $-0.93$  rad/m<sup>2</sup>, the others somewhat less. For our VLA observations, the ‘jplg’-based estimates were always the largest. Closer inspection of the residuals over time shows that these offsets vary only slightly over the length of an observation. The fact that the post-correction residuals are exactly linear as a function of  $\lambda^2$  shows that these estimates have an offset in estimated IFRM, which can only be due to an overestimate in the VTEC maps as the magnetic field models are the same for both local and global estimates..
- The ALBUS IFRM estimates are much closer to the actual IFRM than any of those derived from the global maps. Of the various models available, the G01 model – utilizing a single, nearby, well-calibrated GNSS station – is always the closest to observed values.
- The scatter in the ALBUS estimates about the known zero slope is less than 0.1 rad/m<sup>2</sup>. This represents the evident accuracy of these corrections.

Another way to show the effectiveness of the IFRM corrections is to plot the uncorrected and corrected EVPA values for each scan within a single observation. As noted above, this is only practical for the ‘D2’ and ‘DC’ observations. In Figure 7 we show this for the highly polarized NE hotspot in DA240 and for the Moon for each scan for the D2 observation. The steeply sloping solid lines, whose slopes are the observed RM, show the RM increasing as a function of time, as the rising Sun increases the ionization of the ionosphere. In the left panel, the results of applying the ALBUS model and the global ‘jplg’ estimates to DA240 are shown. The resulting post-correction EVPAs are very consistent over the scans, showing that the increase in IFRM has been effectively removed, but the average corrected slopes are quite different for different IFRM corrections – a result of the offset in IFRM between estimates shown in Figure 5. Deciding which is correct requires knowledge of the true RM for DA240 – which we don’t have, although there is an early result from the WSRT array (M. A. Brentjens 2007) which agrees with the ALBUS result . The right panel shows the same results for the Moon. The SNR is lower, but the lunar observations have the great advantage that we know the correct answer in advance – the corrected slope should be zero (as the Moon and the cis-lunar environment have no IFRM of their own), and the zero-wavelength intercept should be close to zero, indicating the EVPA is purely radial. The right panel shows that the ALBUS corrections do indeed have close to zero slope and zero intercept.

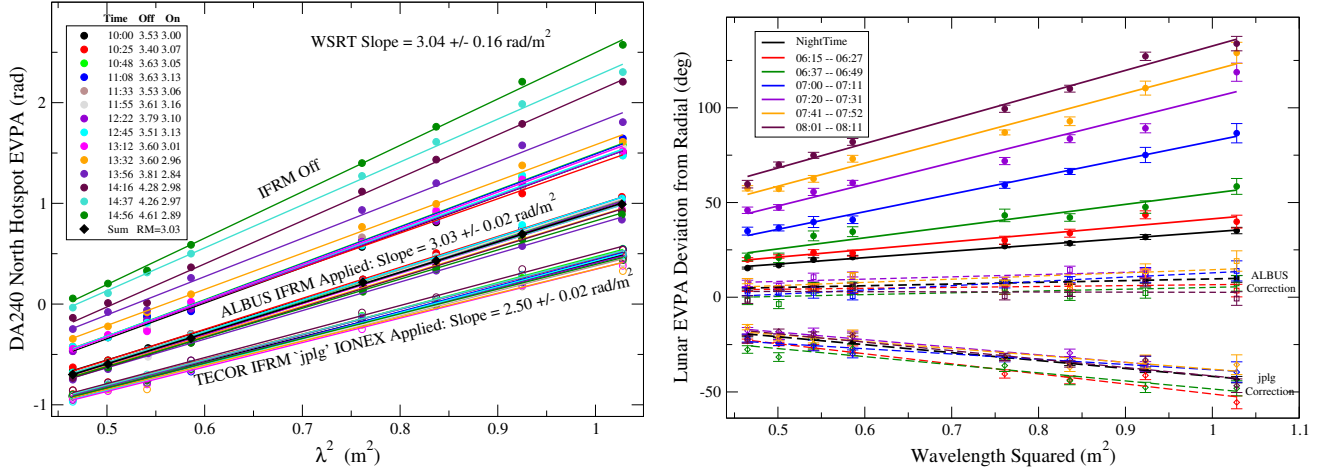


**Figure 7. (Left)** The observed and corrected EVPAs for DA240 for the ‘D2’ observation by time. Shown are the uncorrected, and IFRM-corrected data for two estimates. **(Right)** Same, for the Moon. The colored solid lines show the fits to each observation taken after dawn. The black solid line is the fit for the night-time observations. The dashed lines show the fits following ALBUS corrections (shorter dashes) and ‘jplg’ global (longer dashes)

## 7. MEERKAT RESULTS

MeerKAT is an outstandingly capable instrument for imaging low surface brightness structures. Its centrally condensed array design ( $\sim 40$  of its 64 antennas are within 500 m of the array center) provides very high surface brightness sensitivity on the angular scales of interest for lunar polarimetry. In addition, considerable care has been taken in preventing antenna- and site-generated RFI from causing spurious correlations. Due to its remote site, the external RFI in the UHF band is minimal (in comparison to the VLA’s P-band environment), with less than 3% of the spectrum having to be removed due to RFI.

We have six lunar observations taken with MeerKAT, listed in Table 3, but only the last three are of use for judging the accuracy of IFRM corrections, as the first three were taken overnight during a period of very low and steady IFRM. Two recent observations, taken August 18 and 19, 2025 were arranged to span sunrise, while the latest observation, taken October 30, spanned sunset.

MeerKAT’s array design provides us with outstanding image sensitivity on the arcminute scales needed for this work – for each 8-minute lunar observation, the EVPA estimates for each of the 16 spectral windows are determined with typical  $1\text{-}\sigma$  errors of 0.2 degrees. The resulting error in the determination of the IFRM for each scan is typically  $0.2 \text{ rad/m}^2$ .

### 7.1. IFRM Estimation

As with the VLA observations, we have measured the actual IFRM using the lunar data for each scan for the three latest MeerKAT UHF band observations. These are plotted in Fig 8, along with estimates generated by TECOR using the global VTEC estimates, and those generated by ALBUS, using the closest calibrated GNSS station, at Sutherland.

As with the VLA, the global estimates are always too large (negative for this latitude), although the offset is not as great as with the VLA. We show two ALBUS estimates – both using the well calibrated data from two of the Sutherland sites – ‘suth’ and ‘sutm’. For both of these, receiver bias values are available and have been used by ALBUS. The resulting estimates are a good fit to the data for the two August observations, but are not as good for the October 30 data, where it appears that a sudden change at about 15:30 SAST caused the IFRM estimates to jump upwards by nearly  $0.5 \text{ rad/m}^2$ . The origin of this is unknown to us.

Time-integrated observations of the Moon with various corrections, resulting in estimates of the average error incurred with each estimation over the length of each observation, are shown in Fig 9. Notable here is that residual IFRM values are best for the G01 correction using the well-calibrated receiver ‘sutm’ – with a residual of less than  $0.02 \text{ rad/m}^2$ . The ‘suth’ data results are very similar, but are slightly less accurate, while the ‘global’ estimates always

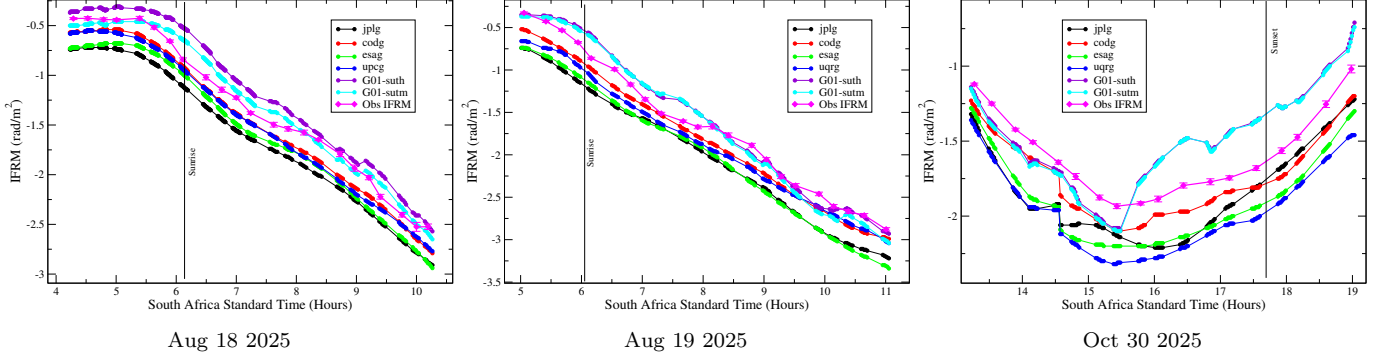


**Figure 8.** The estimated and observed IFRM values for the three MeerkAT observations. For all three, the estimates based on global VTEC maps overestimate the IFRM at all times. The single-station ALBUS estimates are the closest to the observed values, except for the Oct 30 data.

bht

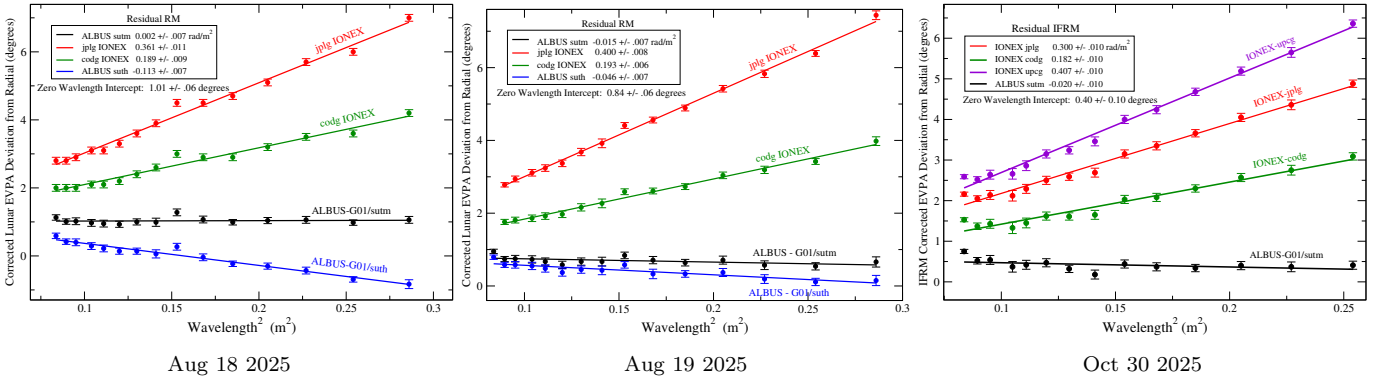


**Figure 9.** Showing the integrated residual EVPA values following IFRM corrections by various estimates. As with the VLA observations, the global VTEC-based estimates overcorrect the EVPA values. The ALBUS estimates based on a single local well-calibrated receiver again give the most accurate corrections.

overcorrect the rotation, although the overcorrection is significantly less than for the VLA observations – typically  $-0.2$  to  $-0.4$   $\text{rad}/\text{m}^2$ .

We show in Figure 10 the detailed before and after EVPA deviations for each 8-minute scan for the two August 2025 observations. This plot shows the raw EVPA offsets with no corrections with solid lines, and the resulting values following correction by the ‘jplg’ global estimation (short dashes), and the local ALBUS correction (long dashes).

## 8. POLARIZATION CHARACTERISTICS FOR 3C286 AND 3C138

A secondary purpose of this work is to determine the polarization characteristics for the standard calibrators 3C286 and 3C138 over the entire frequency range that its polarized emission can be used for correction of the cross-hand phases for circularly polarized receiver systems. Both sources are significantly resolved to the VLA, so care must be taken in utilizing their structures for calibration purposes. Maps of each, utilizing recent JVLA A-configuration observations, are shown in Fig 11.

For both the VLA and MeerkAT, determining the intrinsic polarization structures requires correction for any systematic offsets in the determination of the EVPA. For circularly polarized systems, such an offset will be caused by an incorrect phase offset between the RCP and LCP data – mostly likely due to an incorrect assumption of the EVPA of the polarized calibrator. For linear systems, an offset will occur due to misorientation of the receiver in the antenna used as the phase reference during the calibration process. Other origins of offsets can also be imagined.

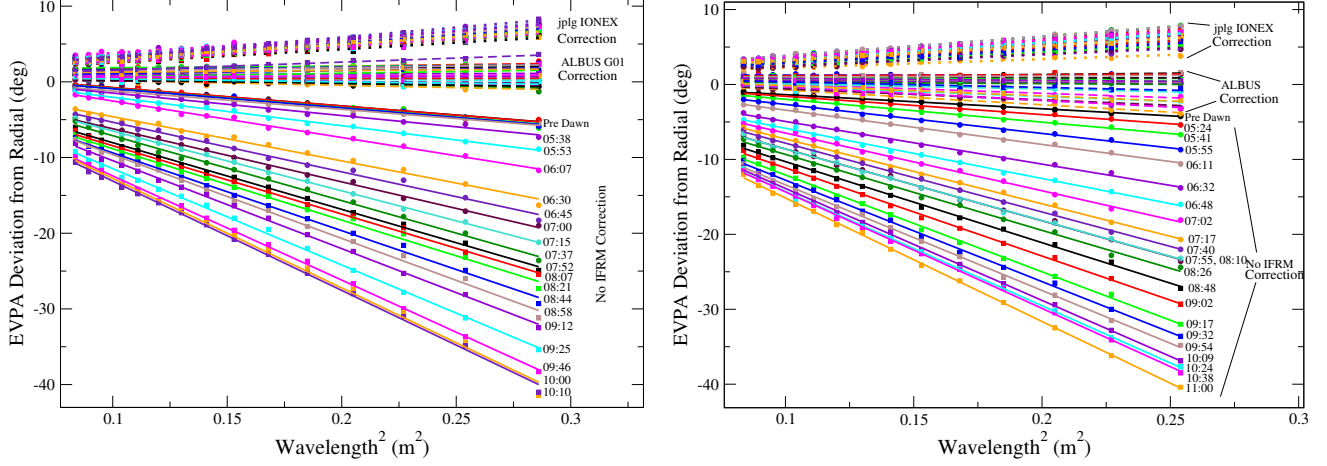


**Figure 10.** Showing the uncorrected observed lunar EVPA offsets, and the values after correction by the ‘jplg’ global estimate and the ALBUS estimate for two MeerKAT observations – 18Aug2025 of the left, and 19Aug2025 on the right.

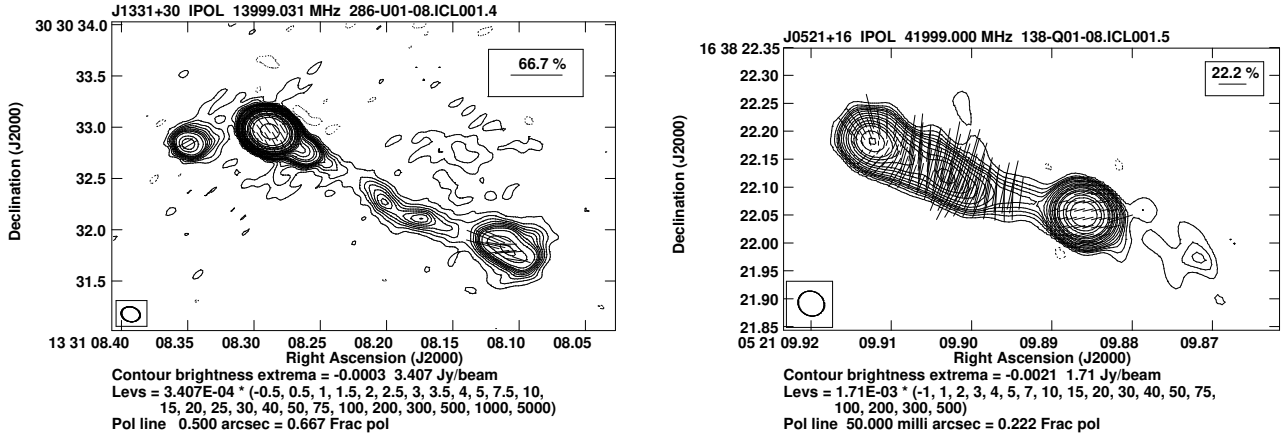


**Figure 11.** Maps of the polarized calibrators 3C286 (left) at 14 GHz with 150 mas resolution, and 3C138 (right) at 42 GHz with 45 mas resolution. For 3C286, both the Stokes I and polarized flux density are dominated by the nuclear emission – the Stokes I extended emission accounts for only 166 mJy compared to 3.58 Jy for the nuclear core. For 3C138, the situation is quite different – the Stokes I extended emission is much stronger, accounting for 571 mJy compared to 1.710 Jy for the nucleus, while the polarized emission at this band is about equal between the jet and the nucleus.

The removal of these offsets can be analyzed in the following way. Let  $\chi$  represent the EVPA for a given position within the polarized image. The observed EVPA,  $\chi_{obs}$ , is related to the true EVPA,  $\chi_{true}$ , by

$$\chi_{obs} = \chi_{true} + RM\lambda^2 + \delta\chi \quad (5)$$

where RM is the actual rotation measure at a given time for the source, and  $\delta\chi$  is any instrumental offset, such as mis-oriented receivers for a linear system, or incorrect cross-hand phase for a circular system. After correction by a model rotation measure  $RM_m$ , the corrected EVPA will be given by

$$\chi_{obs,corr} = \chi_{true} + \Delta RM\lambda^2 + \delta\chi \quad (6)$$

where  $\Delta RM = RM - RM_m$  represents the difference between the true and estimated rotation measure along the line of sight to the source. For a lunar or planetary observation, we interpret  $\chi_{true}$  as the deviation from radial, so  $\chi_{true} = 0$ , giving

$$\chi_{obs,corr,moon} = \Delta RM\lambda^2 + \delta\chi \quad (7)$$

This is the formulation which forms the basis of the analysis done in previous sections.

For a subsequent determination of a calibrator EVPA (where  $\chi_{true} \neq 0$ ), we subtract the planetary residual corrected EVPA determination from the calibrator determination, and presuming the offset  $\delta\chi$  is common to both sources, we find

$$\chi_{true,src} = \chi_{corr,src} + (\Delta RM_{src} - \Delta RM_{moon}). \quad (8)$$

EVPA offsets which are common to both planetary and calibrator observations are removed in this subtraction process. Furthermore, if the IFRM determinations for both target and planet were in error by a constant amount due to a constant offset in the TEC calculation, such offsets will also be removed.

In words, the polarization EVPA values for a target source require a determination of the Stokes Q and U values for both the source and for the planet (Mars, Venus, Moon), with the best IFRM estimates applied. Under the assumption that the offset in the EVPA on the calibration source is constant in time, this offset is subtracted from the EVPA value determined for the target source to give the best estimate of the source EVPA.

### 8.1. 3C286

As noted in the introduction, high frequency VLA polarimetric observations by [R. A. Perley & B. J. Butler \(2013a\)](#) showed that the EVPA of 3C286 increases from 33 degrees at 10 GHz to approximately 36 degrees at 45 GHz. Subsequent observations by high frequency telescopes have confirmed and extended this trend ([M. Kam et al. 2025](#), and references therein). The [R. A. Perley & B. J. Butler \(2013a\)](#) work did not include measurements below 8 GHz, and it was not until early MeerKAT polarimetric observations of 3C286 indicated the EVPA continues to decline from 33 degrees at frequencies less than 6 GHz that further VLA observations were made.

As part of our investigation of IFRM corrections, we have taken more observations with the VLA with the intention of using the same methods described here and in [R. A. Perley & B. J. Butler \(2013a\)](#) to determine the intrinsic EVPAs of standard calibrators, mostly notably 3C286, over the full frequency range that its polarization can be detected. For the VLA’s L-band and the MeerKAT array’s UHF band, ionospheric corrections are essential. The results of our work, over all frequencies, and with both arrays, with ALBUS G01 corrections applied, are shown in Figure 12. As 3C286 and 3C138 are significantly resolved by the VLA in most configurations, these results make use of integrated measures – the I, Q, and U brightnesses are integrated over the source extents to provide the utilized flux densities. Not all

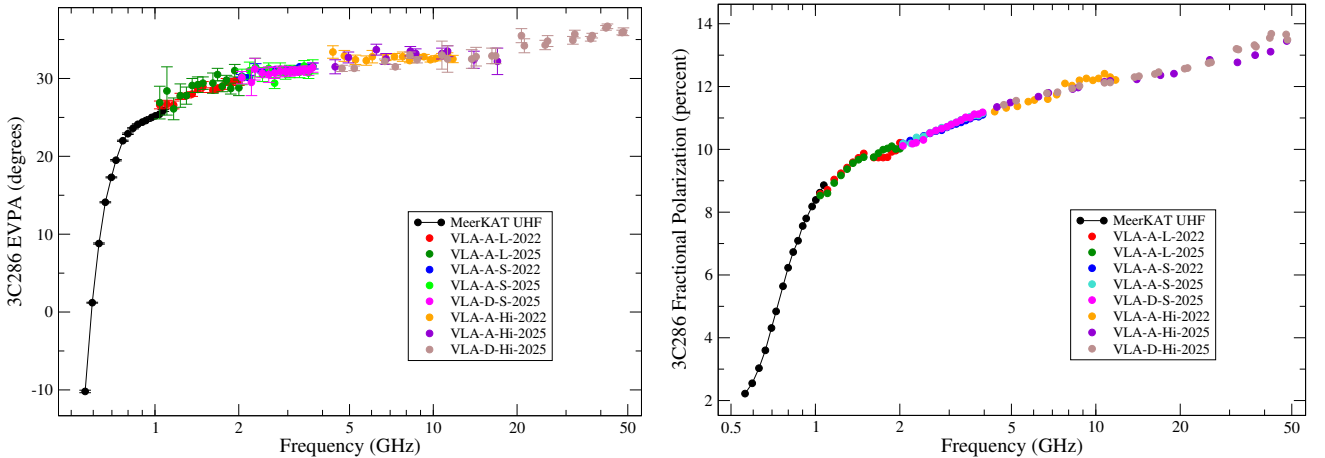


**Figure 12.** Showing the intrinsic EVPA (left) and polarization fraction (right) of 3C286, from VLA and MeerKAT data. These data have been corrected with the ALBUS G01 IFRM estimates. There is excellent agreement between VLA bands, and between MeerKAT and VLA low frequency measurements.

the available data were utilized in this figure. For the VLA, only those observations whose EVPAs are referenced to emission from Venus or Mars were used, as the large angular extent of the Moon causes potential polarization EVPA offsets due to the polarized structure of the VLA’s primary beam. The angular extents of Venus and Mars are small enough that beam polarization contamination is not a limiting issue.

For MeerKAT, we have not used the L and S band observations due to its strongly polarized primary beam structure beyond the half-power point. Furthermore, for the 3C286 polarization measurements, only the 2021 data were used, as the IFRM for that date was very low – less than  $-0.1 \text{ rad/m}^2$  – while for the October 2025 observation, the IFRM

estimates were an unrealistically high  $-6 \text{ rad/m}^2$ , leading to a significant overcorrection of the Faraday rotation for this source. This overestimate is likely due to the very low elevation of 3C286 as seen by MeerKAT combined with an apparently erroneous gradient determination towards the north.

The left panel shows the derived intrinsic EVPA for 3C286 as a function of frequency. There is a very satisfactory agreement between the VLA and MeerKAT results. The EVPA slowly declines from  $\sim 36$  degrees at 48 GHz to a value near 25 degrees at 1 GHz. The fractional linear polarization similarly declines from nearly 14% at 48 GHz to about 8.5% at 1 GHz. Below this frequency, there is a very rapid depolarization and EVPA rotation, such that at the lowest MeerKAT UHF lowest frequency of 540 MHz, the source is polarized at only 2%, with an EVPA near  $-10$  degrees.

To assist accurate polarimetry for all radio telescopes, we provide analytic expressions for the intrinsic EVPA for 3C286. For this purpose, we have smoothed and sampled the data shown in the left panel of Figure 12, then fitted a polynomial as a function of  $\log(\nu_G)$ , where  $\nu_G$  is the frequency in GHz. Simpler expressions are obtained by dividing the frequency span into two ranges: For frequencies between 0.5 and 1.0 GHz

$$EVPA = 26.0 + 57.0x + 615x^2 + 3790x^3 \quad (9)$$

and for frequencies between 1.0 and 50 GHz

$$EVPA = 26.1 + 17.1x - 16.1x^2 + 5.75x^3 \quad (10)$$

where  $x = \log(\nu_G)$ . These expressions fit the smoothed data to better than 0.3 degrees.

## 8.2. 3C138

This highly polarized source is not normally recommended for polarization calibration, as it is highly variable, with strong flares beginning in 2002 and extending through the decade (R. A. Perley & B. J. Butler 2013b), and again in 2025. These flares – which can increase the nuclear flux density at 45 GHz by a factor of four or more – change both the source flux density and polarization, especially at higher frequencies. The variability does not seem to affect the low frequency characteristics by much, as we note the new polarization results below 4 GHz are unchanged from those shown by R. A. Perley & B. J. Butler (2013a). We present here in Fig 13 the results provided by the recent VLA and MeerKAT observations

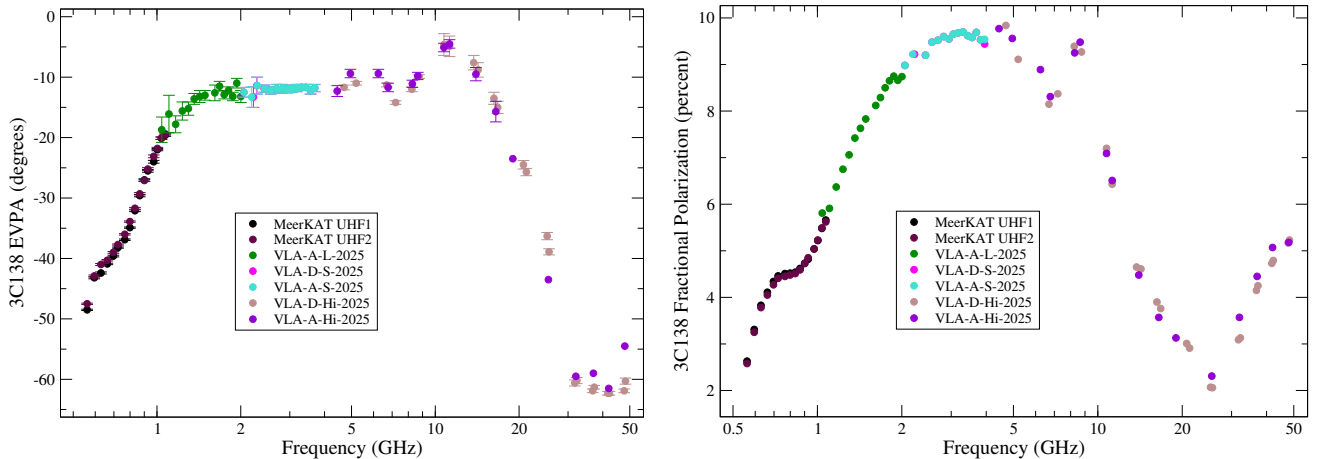


**Figure 13.** Showing the intrinsic EVPA (left) and polarization fraction (right) for 3C138 from VLA and MeerKAT data. These data have been corrected with ALBUS G01 IFRM estimates. The oscillatory behaviour seen above 4 GHz is due to a beating between the nuclear polarized emission and that from the sub-arcsecond jet.

The oscillatory behavior in both the EVPA and the fractional polarization are due to beating between the polarized emission from the extended jet and the nucleus. These oscillations maximize between 10 and 50 GHz as the polarized fluxes from these two components are about equal, but with very different EVPAs. This behavior is not seen below 5 GHz as the inverted spectrum nucleus is too weak to significantly contribute to the total flux density, nor above 50 GHz as the steep-spectrum polarized jet is too weak.

Noting that these oscillations are not seen at frequencies lower than  $\sim 4$  GHz, and also that the derived polarization properties from these recent data are in good agreement with those shown by [R. A. Perley & B. J. Butler \(2013a\)](#) at low frequencies, we conclude that this source remains a useful polarization calibrator for low frequency work.

As for 3C286, we provide analytic expressions for the intrinsic EVPA for 3C138, although for this source, due to its variability, the expressions are only valid below 4 GHz. For this purpose, we have smoothed and resampled the data shown in the left panel of [Figure 13](#), then fitted a polynomial as a function of  $\log(\nu_G)$ , where  $\nu_G$  is the frequency in GHz. Simpler expressions are again obtained by dividing the frequency span into two ranges: For frequencies between 0.5 and 1.0 GHz

$$EVPA = -21.9 + 71.1x - 1435x^2 - 11110x^3 - 23190x^4 \quad (11)$$

and for frequencies between 1.0 and 4.0 GHz

$$EVPA = -22.0 + 95.4x - 340x^2 + 534x^3 - 308x^4 \quad (12)$$

where  $x = \log(\nu_G)$ . These expressions fit the observed data to better than 0.3 degrees.

## 9. SUMMARY

Extensive low-frequency observations of the Moon with the VLA and MeerKAT have provided highly sensitive imaging of the lunar polarization properties, allowing accurate and detailed comparison of the IFRM derived from observations to estimates made from GNSS-based estimates of the STEC. We have compared the observed IFRM-induced variations in EVPA from the known intrinsic radial orientation for the Moon with model estimates generated from published VTEC maps provided by various agencies, and with regional estimates generated by the ALBUS software. From the comparisons we can conclude that for the VLA and MeerKAT:

- All IFRM estimates – both global and regional – show similar changes in IFRM between night and day. These changes closely match the observed changes seen in the lunar and polarized calibrator observations.
- All IFRM estimates generated from global VTEC maps (as implemented by TECOR, RMextract and spinifex) overpredict the IFRM for the VLA observations by 0.5 to 1.0 rad/m<sup>2</sup> for the VLA, and by  $\sim -0.3$  rad/m<sup>2</sup> for MeerKAT, except when the IFRM values are unusually low. These offsets vary between observations, but is roughly constant for any single observation. The thin-shell models using the ‘jplg’ global VTEC maps have the highest overcorrection for all ten VLA observations.
- The estimates provided by the ALBUS program are very close to the measured values. Of the ten ALBUS models available, the G01 model – using only the closest station with known timing bias values, and a simple 2-D (thin-shell) ionospheric model – provides the most accurate and reliable STEC estimates, nearly always within 0.1 rad/m<sup>2</sup> of the actual value. The closest GNSS receiver to the VLA is located at the VLBA Pietown antenna (‘pie1’), 53 km from the VLA, which as part of the IGS service has a well calibrated receiver offset. None of the other GNSS stations within 300 km of the VLA have known offsets. For MeerKAT, the nearest well-calibrated stations are at Sutherland, nearly 200 km away. Despite this distance, use of the station ‘sutm’ alone provides the most accurate estimates of the IFRM.

The origin of the IFRM offsets in the thin-shell models using global VTEC maps is unknown. It must arise from an overestimation of the STEC, or useage of too large a value of the terrestrial magnetic field, or a combination of both. Because the ALBUS G01 model, utilizing a well-calibrated local GNSS station provides an excellent estimate of the IFRM, we believe the more likely explanation is an over-estimation of the VTEC by the global maps. There are references in the geophysical literature to this same conclusion ([Y. Xia et al. 2021](#); [P. Wielgosz et al. 2021](#); [C. Zhao et al. 2021](#)). These papers suggest the overestimation of the VTEC may be due to unmodelled latitudinal gradients. There are also suggestions that the thin-shell model, used in all the implementations utilizing these global VTEC maps, is responsible. [N. K. Porayko et al. \(2019\)](#), and [N. K. Porayko et al. \(2023\)](#), noting the same IFRM overestimates via LOFAR pulsar observations, discuss the possibility that the thin-shell model, combined with an incorrect value of the height at which the electrons are assumed to be, is responsible.

The simple 2-D ALBUS regional model, utilizing a well calibrated nearby receiver, provides the best estimates of the IFRM, suggesting that the problem with the global estimates of VTEC lies with the extensive smoothing required to produce a global map using typically 200-km separated ground stations. This observation leads us to suggest that

much more accurate estimations, in both time and direction, are within reach of ALBUS, or an equivalent program which makes use of local GNSS stations to estimate the STEC, if we can obtain accurate bias values for the  $\sim$  two dozen stations within 300 km of the VLA and MeerKAT sites. Future work should aim at obtaining, or deriving, these bias values, and investigating which of the ten ALBUS models provides the most accurate and reliable IFRM estimates. However, as noted in Appendix B, the internal workings of ALBUS remain a mystery, and it is likely that a significant effort will be required to understand and improve this program.

## APPENDIX

### A. COMPARING RMEXTRACT, SPINIFEX, AND TECOR

There are two alternative programs known to us which provide IFRM estimates – `ionFR` (C. Sotomayor-Beltran et al. 2013) and `RMextract` (M. Mevius 2018). Both of these programs work similarly to TECOR, i.e., using the same model of the Earth’s magnetic field, thin-shell approximation, and global VTEC maps. `ionFR`<sup>7</sup> is no longer maintained. `RMextract` has recently been superseded by `spinifex`<sup>8</sup>(M. Mevius et al. 2025), which is under development for use with LOFAR and SKA-LO observations, both of which operate at wavelengths longer than 1 meter.

To compare the `RMextract`, `spinifex`, and `TECOR` estimates, we show in Fig 14 the lunar IFRM estimates for the D2 observation using the ‘jplg’ and ‘uqrg’ VTEC maps. The uqrg maps are generated by the Polytechnic University of Catalonia, and differ from the upcg maps by being estimated on a 15-minute cadence, rather than the two hours of upcg and jplg.

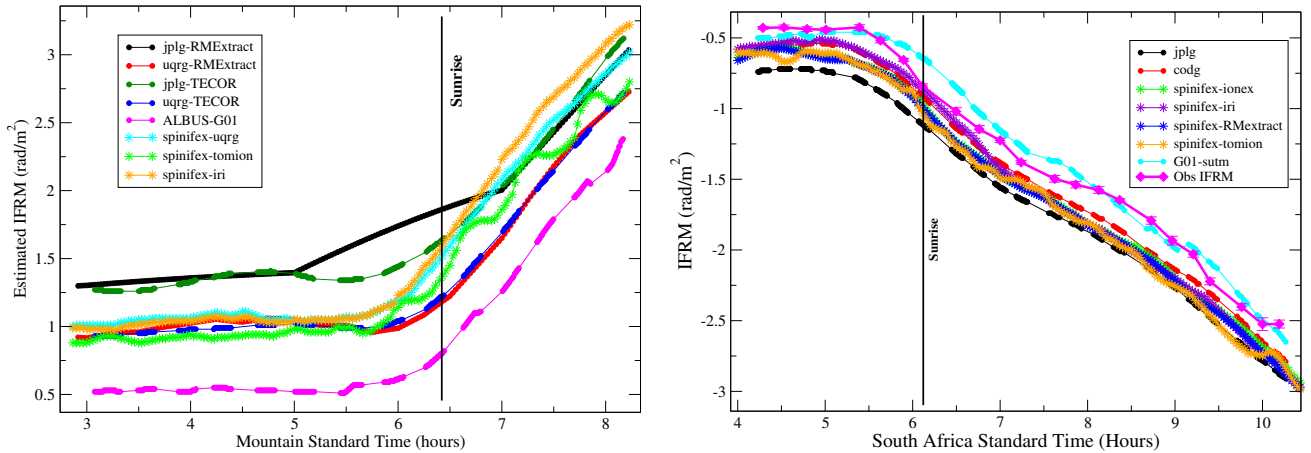


**Figure 14.** Comparing the IFRM estimates provided by TECOR, `RMextract`, ALBUS and `spinifex` for the D2 observation. (Left) For the VLA ‘D2’ observation on 04 November 2023. The ALBUS values, in magenta, are an excellent match to the observed IFRM values. All models based on global VTEC estimates overcorrect the IFRM by 0.5 to 1.0  $\text{rad/m}^2$ . (Right) For the MeerKAT observation on 18 August 2025. The observed IFRM is in magenta, the G01-sutm estimate in blue. All models based on VTEC maps again overestimate the IFRM, although by less than for the VLA – about  $-0.3 \text{ rad/m}^2$ .

The VLA results for the ‘D2’ observation are shown in the left panel. TECOR, using the jplg VTEC map, provides the IFRM estimates shown in green. The black trace shows the `RMextract` solutions using the same jplg VTEC map. It will be noted there is agreement between them once every two hours, at the times at which the map values are defined. The difference between the two is in how they interpolate between map times. TECOR rotates the map following the sun’s movement, effectively assuming the ionospheric profile is fixed to the subsolar point. It appears that `RMextract` simply interpolates between the fixed-time values, ignoring solar movement.

ASTRON recommends the use of the ‘uqrg’ VTEC maps for IFRM estimates. There is also some evidence in the ionospheric literature that it is the most accurate of the global maps (see, e.g., P. Wielgosz et al. (2021) and C. Zhao et al. (2021).) The TECOR and `RMextract` estimates using this map are shown in the blue (TECOR) and red

<sup>7</sup> <https://github.com/csobey/ionFR>

<sup>8</sup> <https://git.astron.nl/RD/spinifex>

**Table 6.** Description of ALBUS Ionosphere Models

Model	Description
G00	Single station, nearest satellite
G01	Single station, simple 2D, all satellites
G02	Multiple stations, simple 2D, all satellites
G03	Multiple stations, 3D model (same long, lat for all h)
G04	Multiple stations, 3D model (different long, lat for all h)
G05	Multiple stations, 3D model (spherical harmonics with different h layers)
G06	Multiple stations, 2D model with time dependence
G07	Multiple stations, 2D model with gradient least squares
G08	Multiple stations, 2D model with time, gradient least squares
G09	Multiple stations, 2D model with spherical, gradient least squares

(RMextract) traces. The issue of interpolation is largely avoided here because of the 15-minute cadence of the uqrg maps. Close inspection of the red trace shows the inflection points every 15 minutes, corresponding to the times at which the maps are updated. The agreement with TECOR is now very good. The ASTRON recommendation is likely based on both this, and on the observation that the IFRM offset is less for the uqrg maps than for the jplg maps.

For comparison, the ALBUS model prediction, which matches closely the observed IFRM values, is shown in magenta, significantly less than either IONEX model, as already noted. Also shown are three estimates by the successor to RMextract – spinifex.

The MeerKAT results for 18 August 2025 are shown in the right panel. For this instrument, the differences between models are much less than for the VLA – typically less than  $0.3 \text{ rad/m}^2$ . But the same trends as for the VLA are evident – all estimates based on global VTEC maps overcorrect (here, in the negative sense) the IFRM, while the G01-sutm estimate is the closest to the observed values – despite the nearly 200 km separation of that station from the MeerKAT array.

## B. MORE DETAILS ON ALBUS

ALBUS generates an estimate of the IFRM for a given time, location and direction by utilizing available nearby GNSS station data. The current version of ALBUS utilizes only GPS data, although the program can potentially utilize the data from at least two other satellite constellations. The version utilized in this paper allows specification of the desired stations to be polled, as well as a maximum distance for the stations from the desired location.

Following retrieval of these datasets, ALBUS polls the ‘codg’ IGS data to obtain the satellite and receiver timing bias values. As noted below, knowledge of these values is critical in obtaining accurate IFRM estimates. If no station bias values are found, the uncorrected data are used.

Following data retrieval and calibration, the observed differential times between two frequencies within L-band are converted to total electron column density for each of the satellites within view. From these are derived a time-dependent map of the TEC for the entire hemisphere, from which the STEC for the source of interest is derived. ALBUS offers ten different ionospheric models, briefly described in Table 6, including both 2- and 3-dimensional distributions of the electron density.

An important aspect of utilizing GNSS data is the issue of satellite and receiver biases. Each transmitter, and each receiver, has its own timing offset. These biases are of the same magnitude as the actual dispersive timing differences used in the calculation of the STEC (see [W. C. Erickson et al. \(2001\)](#) for examples) – hence it is of considerable importance that these be removed from the raw data. In Figure 15 we show in the left panel the estimated STEC (using the G01 model and selecting the single-station option) for the three individual GNSS stations closest to the VLA: ‘pie1’ is located at the VLBA site near Pietown NM, 52 km from the VLA at azimuth  $-62$ , ‘sc01’ is on top of Socorro Peak, 60 km from the VLA at azimuth 91, and ‘p107’ is near Grants NM, 120 km from the VLA at azimuth  $-12$ . Of these three, only the ‘pie1’ station has a known receiver bias, which has been applied in the calculations. The biases for the other two stations are not known, and the values in the plot reflect this lack. The right-hand panel

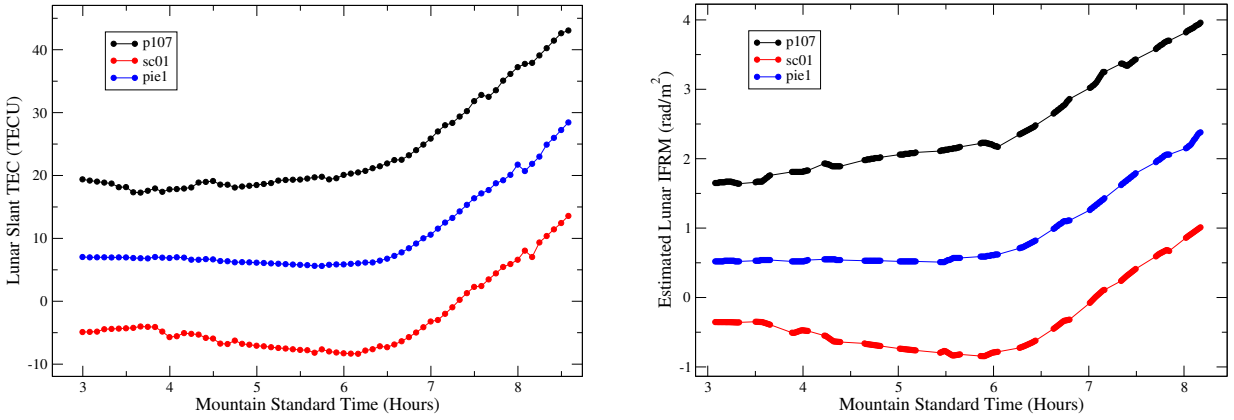


**Figure 15.** Showing STEC (left) and IFRM (right) estimates using data from the closest three GNSS stations to the VLA for the VLA D2 observation. Only the ‘pie1’ station (blue traces) has known receiver bias values. Use of the data from the other two stations results in improbable, or impossible, estimates of the STEC and IFRM.

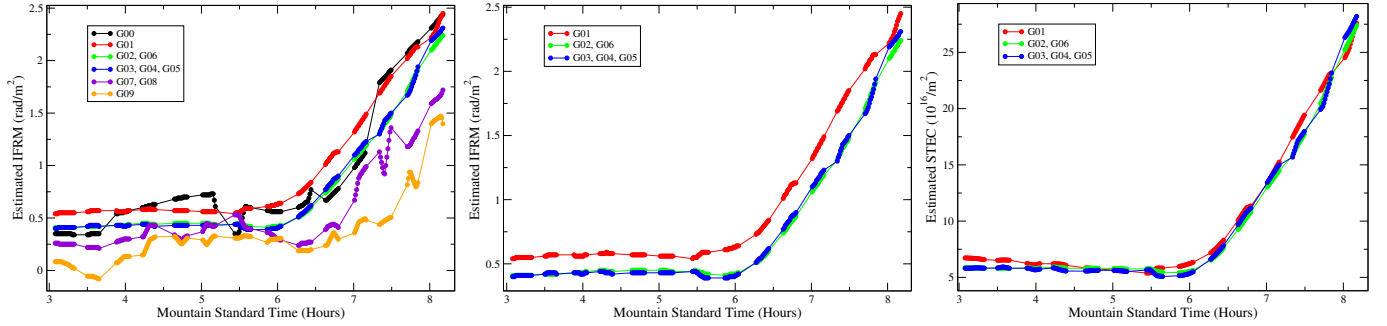


**Figure 16.** Showing the ALBUS estimates of IFRM and STEC for the ‘D2’ observation. (Left) The estimated IFRM for all ten models. (Center) The estimated IFRM for the six stable models. Note that the estimate for the G01 model is higher than the others, and closely matches the observed lunar values. (Right) The STEC for the six stable models. Note that although all stable models have similar values of STEC, the ALBUS code estimates different values of IFRM.

shows the resulting estimates of the IFRM. As noted in this paper, the blue trace (‘pie1’) closely matches the observed IFRM determined from the lunar observations.

The large differences between estimates emphasizes the importance of including bias values. Note that the ‘sc01’ data estimates a negative electron column density, and a negative IFRM – both are physical impossibilities.

As part of this work, we investigated the characteristics of each of these models, using the ‘D2’ observations. The estimated IFRM values of all ten models for the ‘D2’ data are shown in the left panel of Fig 16. For this example, we have used a GNSS station search of 165 km, since use of a single station causes the ‘3-d’ models G03, G04, and G05 to generate impossible values of the IFRM. From this plot we see that the G02 and G06, G03, G04, and G05, and the G07 and G08 estimates are identical. The G00, G07, G08, and G09 estimates are unstable, and we do not consider these further. The stable G01 through G06 IFRM estimates are shown in the center panel of the figure. Note that the G01 estimate is higher than the others, which are all very similar. As noted in this paper, the G01 estimate closely matches the observed IFRM values determined from the lunar observations, while the others, although similar, are significantly lower. In the right-hand panel, we show the estimated STEC values used to generate the IFRM values shown in the middle panel. Surprisingly, all STEC values are very similar – the clear higher value in IFRM from the G01 model is not reflected in the STEC values. We do not understand how this can be – the conversion from STEC to IFRM involves integration of the product of the STEC distribution with the line-of-sight values of the magnetic field. Presuming the program uses the same magnetic field model for this computation, the estimated IFRM values should reflect the STEC values – especially for the G01 and G02 models, both of which presume a 2-d electron distribution – the thin-shell model.

This apparent discrepancy illustrates a problem with the ALBUS program – we don’t understand in detail what its internal computations are doing. The program is large and complex, with a Python layer on top of lower level C and C++ software. See Willis, A. (2022) for details. Other tests that we have performed show characteristics that are not understood. What we can state with certainty is that the the simple G01 model, using a single nearby station with known receiver bias values, provides the best estimates of the IFRM. But we do not understand why a simple 2-D (thin-shell) model gives better results than a full 3-D model, which physically we would expect to give better results. Further progress will require a detailed examination of the code, with a goal of implementing the more sophisticated models using high-quality GNSS data with known receiver biases.

#### ACKNOWLEDGMENTS

The MeerKAT telescope is operated by the South African Radio Astronomy Observatory, which is a facility of the National Research Foundation, an agency of the Department of Science and Innovation.

The National Radio Astronomy Observatory and Green Bank Observatory are facilities of the U.S. National Science Foundation operated under cooperative agreement by Associated Universities, Inc.

This work has made use of the ‘MPIfR S-band receiver system’, designed, constructed, and maintained by funding of the MPI für Radioastronomie and the Max-Planck Society.

We thank Joe Helmboldt and Anthea Coster for helpful advice on ionospheric physics, and for providing ionosonde and MADRIGAL data for comparison to the global VTEC estimates. We thank the anonymous referee for useful comments on the original text.

#### AUTHOR CONTRIBUTIONS

RAP set up the observations, calibrated the data, analyzed the results, and led the paper writing. BJB provided essential information on ionospheric modelling and on the use of planetary bodies for polarimetric calibration. ET developed the containers for running ALBUS within the AIPS environment. EWG implemented many changes within AIPS to enable the imaging, and implemented the container needed to run ALBUS within the AIPS environment. BVH facilitated the MeerKAT lunar observations, and provided advice for accessing trignet data. AGW provided essential advice on the ALBUS program, and implemented many modifications to speed up its execution and to improve its capabilities and user interface. All authors contributed to the writing and editing of this paper.

*Facilities:* NRAO (VLA), SARAO (MeerKAT)

*Software:* AIPS (E. W. Greisen 2003), ALBUS ( Willis, A. 2022), RMextract (M. Mevius 2018), spinifex (M. Mevius et al. 2025)

#### REFERENCES

- Alken, P., Thébaud, E., Beggan, C. D., et al. 2021, Earth, Planets and Space, 73, 49, doi: [10.1186/s40623-020-01288-x](https://doi.org/10.1186/s40623-020-01288-x)
- Brentjens, M. A. 2007, PhD thesis, University of Groningen, Netherlands
- Chapman, S., & Bartels, J. 1940, Geomagnetism, Vol. I: Geomagnetic and Related Phenomena
- Erickson, W. C., Perley, R. A., Flatters, C., & Kassim, N. E. 2001, A&A, 366, 1071, doi: [10.1051/0004-6361:20000359](https://doi.org/10.1051/0004-6361:20000359)
- Greisen, E. W. 2003, in Astrophysics and Space Science Library, Vol. 285, Information Handling in Astronomy - Historical Vistas, ed. A. Heck, 109, doi: [10.1007/0-306-48080-8\\_7](https://doi.org/10.1007/0-306-48080-8_7)
- Heiles, C. E., & Drake, F. D. 1963, Icarus, 2, 281, doi: [10.1016/0019-1035\(63\)90023-X](https://doi.org/10.1016/0019-1035(63)90023-X)
- Kam, M., Nagai, H., Kino, M., et al. 2025, ApJ, 994, 196, doi: [10.3847/1538-4357/ae10b1](https://doi.org/10.3847/1538-4357/ae10b1)
- Lawrence, R. S., Little, C. G., & Chivers, H. J. A. 1964, IEEE Proceedings, 52, 4, doi: [10.1109/PROC.1964.2737](https://doi.org/10.1109/PROC.1964.2737)
- Mevius, M. 2018, RMextract: Ionospheric Faraday Rotation calculator,, Astrophysics Source Code Library, record ascl:1806.024 <http://ascl.net/1806.024>

- Mevius, M., Thomson, A., & Dijkema, T. J. 2025, spinifex, 1.0 Zenodo, doi: [10.5281/zenodo.15000430](https://doi.org/10.5281/zenodo.15000430)
- Perley, R. A., & Butler, B. J. 2013a, ApJS, 206, 16, doi: [10.1088/0067-0049/206/2/16](https://doi.org/10.1088/0067-0049/206/2/16)
- Perley, R. A., & Butler, B. J. 2013b, ApJS, 204, 19, doi: [10.1088/0067-0049/204/2/19](https://doi.org/10.1088/0067-0049/204/2/19)
- Perley, R., & Greisen, E. 2024, Post-Correlation Basis Conversion in AIPS, EVLA Memo Series #229, [https://library.nrao.edu/public/memos/evla/EVLAM\\_229.pdf](https://library.nrao.edu/public/memos/evla/EVLAM_229.pdf) NRAO
- Perley, R., Greisen, E., & Hugo, B., Enabling MeerKAT Polarimetric Imaging in AIPS, EVLA Memo Series #219, [https://library.nrao.edu/public/memos/evla/EVLAM\\_219.pdf](https://library.nrao.edu/public/memos/evla/EVLAM_219.pdf) NRAO
- Porayko, N. K., Noutsos, A., Tiburzi, C., et al. 2019, MNRAS, 483, 4100, doi: [10.1093/mnras/sty3324](https://doi.org/10.1093/mnras/sty3324)
- Porayko, N. K., Mevius, M., Hernández-Pajares, M., et al. 2023, Journal of Geodesy, 97, 116
- Sotomayor-Beltran, C., Sobey, C., Hessels, J. W. T., et al. 2013, A&A, 552, A58, doi: [10.1051/0004-6361/201220728](https://doi.org/10.1051/0004-6361/201220728)
- Wielgosz, P., Milanowska, B., Krypiak-Gregorczyk, A., & Jarmolowski, W. 2021, GPS Solutions, 25, 103, doi: [10.1007/s10291-021-01142-x](https://doi.org/10.1007/s10291-021-01142-x)
- Willis, A. 2022, ALBUS: Determination of the ionosphere total electron content (TEC) over any location on the Earth as a function of location and time., v1.0.0, [https://github.com/twillis449/ALBUS\\_ionosphere](https://github.com/twillis449/ALBUS_ionosphere) GitHub
- Xia, Y., Meng, X., Yang, Y., et al. 2021, Satellite Navigation, 2, 8, doi: [10.1186/s43020-021-00035-1](https://doi.org/10.1186/s43020-021-00035-1)
- Zhao, C., Gong, W., Li, T., et al. 2021, Engineering Geology, 288, 106138, doi: <https://doi.org/10.1016/j.enggeo.2021.106138>
- Zhao, Q., Zhang, K., & Yao, W. 2019, Annales Geophysicae, 37, 15, doi: [10.5194/angeo-37-15-2019](https://doi.org/10.5194/angeo-37-15-2019)